# Estimations of edge plasma and impurity performance on HL-2M with EMC3-EIRENE modelling

Z. Liang[1, *], S.Y. Dai[1, *], Y. Feng[2] and D.Z. Wang[1]

[1] *Key Laboratory of Materials Modification by Laser, Ion and Electron Beams (Ministry of Education), School of Physics and Optoelectronic Technology, Dalian University of Technology, Dalian 116024, China*
[2] *Max-Planck-Institut für Plasmaphysik, D-17491 Greifswald, Germany*

E-mail: daishuyu@dlut.edu.cn and wangdez@dlut.edu.cn

## Abstract

The three-dimensional edge transport code EMC3-EIRENE has been employed to investigate the edge plasma behavior and carbon impurity transport in the HuanLiuqi-2M (HL-2M) tokamak. It is found that the outboard divertor target has a narrower flux deposition width and therefore undergoes more intense peak heat flux than the inboard one. Detailed analysis of carbon impurity has been performed to obtain deeper insights into the mechanisms of edge impurity transport and mitigation of heat loads. Detailed analyses of carbon impurity have been performed to obtain deeper insights into the mechanisms of edge impurity transport and mitigation of heat loads. As the increment in upstream density, a larger region in the intrinsic friction force dominant regime has been achieved in divertor region, while less impurity ionization source locates in the thermal force dominant region, and hence a better impurity screening has been obtained. The total power loss induced by carbon impurity shows no significant differences as the upstream density increases when it is higher than $1.5\times10^{19}$ $m^{-3}$, even though the total number of carbon ions in space obviously decreases. Further study on impacts of the impurity source locations has been performed. The carbon impurity eroded from the vertical part of the outboard target is likely to leak out into the upstream, which is attributed to that the region where the intrinsic friction force dominates is thin. On the other hand, the carbon impurity eroded from the inboard target and the horizontal part of the outboard target is under good control due to the wider region in the intrinsic friction force dominant regime.

Keywords: edge plasma, heat loads, impurity transport, HL-2M

## 1. Introduction

The optimization of the heat flux depositions on divertor targets and the control of impurity are considered to be important for operation and performance of magnetically confined fusion devices. [1-3]. High heat flux deposition aggravates the erosion of target materials, and hence, degrades the performance and reduces the lifetime of the divertor [4-6]. Further, the leakage of eroded impurity into the upstream can lead to degradation of energy confinement of fusion devices, or even terminate the discharge [7]. On the other hand, the power exhaust by impurity radiation in divertor region can mitigate the heat loads on divertor targets [8-12] and contribute to the achievement of detachment [13-16]. Hence,

* These authors contributed equally to this work and should be considered co-first authors.

investigations of the heat loads and impurity transport behavior are beneficial for the long-term, high performance operation of fusion facilities.

The numerical simulations of edge plasma and impurity behaviors are essential for the new fusion devices, which can check the baseline of operation parameters and predict the preferable scenarios for future operation. Recently, a new tokamak HL-2M [17] has been constructed and the first discharge has been performed in the Southwestern Institute of Physics (SWIP). In our previous study [18], the edge plasma properties and heat loads on the divertor targets have been studied for the pure deuterium plasma scenario. Additionally, the preliminary analysis demonstrated that the intrinsic carbon impurity contributes to the reduction in heat loads, while the impacts of carbon impurity to edge plasma and the mechanisms of power exhaust were not investigated in detail. Additionally, the extrinsic gas puffing will be explored to study the impurity transport behavior and its impacts on the heat load in future experimental projects on HL-2M. The studies of the extrinsic gas puffing necessitate the three-dimensional (3D) modelling due to the broken toroidal symmetry. Before that, one should understand the impacts of intrinsic carbon impurity to edge plasma and the mechanisms of power exhaust on HL-2M. Hence, the 3D code EMC3-EIRENE has been employed here to study the transport behaviors of intrinsic carbon impurity in order to keep consistency with future modelling of extrinsic gas puffing. The EMC3-EIRENE code has a good flexibility for switching on/off the impurity source on divertor targets, which enables us to make a study on impacts of impurity source locations later shown in this work.

In this work, the further simulations with the carbon impurity under different edge plasma conditions have been attempted. Besides the assessments of edge plasma properties, the detailed analyses on the carbon impurity transport and its power exhaust property have been performed. The force balance between the ion thermal force and the friction force has been investigated and an expansion of friction dominant region is achieved with lager upstream density ($n_{eu}$), which leads to a better impurity screening. The study on the impacts of impurity source location reveals that the carbon impurity released from the vertical part of the outboard divertor target is more likely to leak out into the upstream. The carbon impurity total power loss efficiency is enhanced with the increment in the upstream electron density. Hence, for the scenarios with $n_{eu} \geqslant 1.5 \times 10^{19}$ m$^{-3}$, the power exhaust by carbon impurity maintains a stable magnitude with the increment in $n_{eu}$, though the total number of carbon ions in space decreases obviously.

In section 2, an introduction of HL-2M tokamak and magnetic configuration in this work is presented. Section 3 briefly describes the EMC3-EIRENE code. The detailed simulation results are presented and discussed in section 4. Finally, summary is given in section 5.

## 2. HL-2M tokamak

HL-2M is a new tokamak under construction at SWIP in Chengdu, China, which has been implemented with a plasma major radius of 1.78 m and a minor radius of 0.65 m. It is designed with a heating power of 4~15 MW by composite heating systems including neutral beam injection (NBI), electron cyclotron resonance heating (ECRH), and low hybrid heating (LHH) for routine operation. The toroidal field coils (TFCs) can operate with a maximum field of 2.2 T at plasma center R = 1.78 m [19]. The maximum plasma current is designed to be 3 MA on HL-2M. Carbon fiber composite (CFC) is employed on the actively cooled divertor as plasma facing material (PFM), which supports a heat load tolerance up to 10 MW/m$^2$ [20].

## 3. EMC3-EIRENE code

The 3D edge transport code EMC3-EIRENE [21,22] has been widely employed on simulations of edge plasma and impurity transports [23-29]. The EMC3 code solves a set of time-independent Bragnskii's fluid equations [30] for particles, momentum, energy transports of ions and electrons with Monte Carlo (MC) method, and is coupled with the EIRENE code [31], which is employed to treat the transports of neutral atoms and molecules by solving Boltzmann equation for kinetic transport of atoms and molecules. In EMC3 code the parallel transports along the magnetic field are considered to be classical, while the cross–field transports are assumed to be anomalous and the transport coefficients ($D_\perp$, $\chi_\perp$) are user-specified.

The impurity transport is treated with a trace approximation model [21]. The continuity and momentum equations of impurity transport are involved in EMC3 code while the impurities are assumed to have the same temperature as the main fuel. The parallel transport is determined by the competition between the friction and ion thermal forces [32], while the cross-field transport is also assumed to be anomalous, which has a coefficient ($D_{imp}$) equal to the main plasma $D_\perp$ in this work. The drift and current effects are not included in the EMC3 code. The power losses due to excitation and ionization are computed in EMC3, which are included into the energy balance as energy sinks.

## 4. EMC3-EIRENE simulation of HL-2M

### 4.1 Setup of the EMC3-EIRENE simulation

In this work, the H-mode plasma is simulated, and the plasma current and toroidal field are 2.0 MA and 2.2 T, respectively. Figure 1 (a) shows a poloidal cross-section of computational mesh. The contour plot of the connection

length is presented in figure 1 (b). The connection lengths are less than 50 and 20 m in the SOL and private region, respectively. A zoom-in view of the connection length in the divertor region is shown in figure 1 (c). The magnetic flux tubes have a wider expansion at the inboard divertor leg region than that at the outboard one, which are emphasized with circles. The difference in the connection length leads to differences in plasma parameters, and further, impacts the impurity transport, which will be analyzed in detail in subsection 4.3.

The input parameters for EMC3-EIRENE in this work are specified according to the designed operation baseline of HL-2M. The upstream position is fixed at the normalized poloidal magnetic flux of $\Psi_N \approx 0.95$ in the study as the inner radial boundary at the upstream region. Here $\Psi_N = (\Psi - \Psi_{ax})/(\Psi_{sep} - \Psi_{ax})$, where $\Psi_{ax}$ and $\Psi_{sep}$ are the poloidal magnetic fluxes at the axis and the separatrix, respectively. The $n_{eu}$ has been scanned from $1.0\times10^{19}$ to $3.5\times10^{19}$ $m^{-3}$. The input powers flowing through the inner radial boundary ($\Psi_N \approx 0.95$) of all scenarios are fixed to 4 MW, which is equally split into ions and electrons. The anomalous diffusion and heat transport coefficients are assumed to be $D_\perp = 0.3\,m^2s^{-1}$ and $\chi_\perp = 0.3\,m^2s^{-1}$, respectively. The simulated near-SOL heat flux width is about 2.0 mm by the Eich's fitting equation, which matches the multi-machine regression scaling [33]. In addition, the carbon impurity has a cross-field transport coefficient predefined as $D_{imp} = 0.3\,m^2s^{-1}$ [34,35]. The Bohm sheath boundary condition is applied at the divertor target plates, where the ion and electron sheath heat transmission coefficients are assumed to be 2.5 and 4.5, respectively [32]. In this study, the carbon impurity source is induced by erosion of the divertor target plates. The inverse correlation between chemical sputtering yield and incident flux on the divertor targets has been established in the Ref. [36]. On the other hand, the physical sputtering yield decreases with the diminution of divertor plasma temperature. Hence, the total sputtering coefficient decreases with the increment of $n_{eu}$. Table 1 gives the specified values of total sputtering coefficient for different scenarios. The released neutral carbon impurities are presumed with initial energies of 0.05 eV and 2.0 eV for chemical erosion and physical sputtering, respectively [11]. Additionally, the same sputtered fluxes are supposed for chemical erosion and physical sputtering for easy comparison of their individual contributions, i.e. the same sputtering coefficients $Y_{chemical} = Y_{physical} = \frac{1}{2}Y$, where $Y_{chemical}$ and $Y_{physical}$ are the chemical erosion and physical sputtering coefficients respectively and Y is the total sputtering coefficient given in Table 1. The released carbon impurity flux is determined by the specified sputtering coefficient and the deuterium incident flux.

### 4.2 The edge plasma behavior and heat loads with different $n_{eu}$

Figure 2 shows the poloidal distributions of the edge electron density ($n_e$) and temperature ($T_e$) for the scenarios with $n_{eu}$ being $1.0\times10^{19}$ and $3.0\times10^{19}$ $m^{-3}$. The peak value of $n_e$ is less than $1.2\times10^{19}$ $m^{-3}$ in the divertor regions as shown in figure 2 (a). However, when the $n_{eu}$ increases to $3.0\times10^{19}$ $m^{-3}$, the peak value of $n_e$ in divertor regions increases rapidly to more than $1.5\times10^{20}$ $m^{-3}$ as shown in figure 2 (c). On the other hand, $T_e$ in the divertor region has been obviously suppressed by larger $n_{eu}$. It can be seen from figures 2 (b) and (d) that the $T_e$ near the X-point reduces from 120 eV to 50 eV as the $n_{eu}$ increases from $1.0\times10^{19}$ $m^{-3}$ to $3.0\times10^{19}$ $m^{-3}$. Further investigations based on the parameter scan of the $n_{eu}$ has been carried out in the following.

Figure 3 presents the average values of electron densities and temperatures close to the in- and out- board divertor targets ($n_{ed}$, $T_{ed}$), as functions of $n_{eu}$. The reference lines of $n_{ed} \sim n_{eu}$ and $n_{ed} \sim n_{eu}^3$ are also added in figure 3 (a). For $n_{eu} = 1.0\times10^{19}$ $m^{-3}$, the $n_{ed}$ is no more than $0.7\times10^{19}$ $m^{-3}$, which indicates the divertor plasma is in the low-recycling regime. For $n_{eu} = 1.5\times10^{19}$ $m^{-3}$, the modelled $n_{ed}$ exceeds the curve of $n_{ed} \sim n_{eu}$, which suggests the high-recycling regime has been triggered. At the same time, the $T_{ed}$ is strongly suppressed by the enhanced $n_{eu}$ as shown in figure 2 (b). The $T_{ed}$ is approximately 120 eV for $n_{eu} = 1.0\times10^{19}$ $m^{-3}$, which rapidly decreases to about 50 eV when the $n_{eu}$ increases to $1.5\times10^{19}$ $m^{-3}$. The continual increase of the $n_{eu}$ leads to strong increase in $n_{ed}$ and reduction in $T_{ed}$ in figures 3 (a) and (b), respectively. For $n_{eu} = 1.5\times10^{19}$~$2.5\times10^{19}$ $m^{-3}$, the modelled $n_{ed}$ values approximatively obey the relation of $n_{ed} \sim n_{eu}^3$, which is the typical relation in high-recycling regime [23]. While for $n_{eu} \geqslant 2.5\times10^{19}$ $m^{-3}$, the modelled $n_{ed}$ values deviate from the curve of $n_{ed} \sim n_{eu}^3$. On the other hand, the $T_{ed}$ becomes lower than 10 eV when the $n_{eu}$ is higher than $3.0\times10^{19}$ $m^{-3}$ in figure 3 (b). The further increase in $n_{eu}$ perhaps leads to a rollover of plasma density and particle flux, which are commonly observed in the detachment regime.

Figures 4 (a) and (b) are the distributions of heat flux depositions on the in- and out- board divertor targets, respectively. The horizontal axis is the distance from the position on the target plates to the corners as indicated in figure 1 (a). It can be found in figure 4 (a) and (b) that the deposition width of the outboard target is smaller than the inboard one, and thus, the outboard divertor target is faced with more severe challenge in controlling heat loads. Additionally, the heat flux profiles on the in- and out- board divertor targets mapped to the outside midplane for $n_{eu} = 1.0$ and $3.0\times10^{19}$ $m^{-3}$ has also been displayed in figures 4 (c) and (d) in order to clearly show the difference at the two targets. The enhanced $n_{eu}$ leads to an effective suppression in the heat loads on the divertor targets. The peak values of heat flux

deposition on the divertor targets against the $n_{eu}$ are presented in figures 4 (e) and (f) with the red lines. The peak value of heat loads on the inboard divertor targets reduces from about 7.0 to 3.9 MW/m$^2$ as the $n_{eu}$ increases from $1.0\times10^{19}$ to $3.5\times10^{19}$ m$^{-3}$, which drops by about 44%. The increase in $n_{eu}$ from $1.0\times10^{19}$ to $3.5\times10^{19}$ m$^{-3}$ leads to a reduction in the peak value of heat loads on the outboard divertor targets from 13.8 to 7.3 MW/m$^2$, i.e. the peak value reduces about 47%.

### 4.3 Distributions of carbon impurity

According to the previous studies [8,37-39], the impurity leakage or rentantion is governed by the impurity velocity and the impurity ionization source location. Figure 5 displays the 2D distributions of the impurity parallel velocity ($v_z \approx |V_{||}^{fric}| - |V_{||}^{ther}|$). The intrinsic friction velocity $V_{||}^{fric}$ is driven by the intrinsic friction force and has a direction towards the divertor targets [8]. The thermal velocity $V_{||}^{ther}$ is driven by the thermal force, which has a direction away from the divertor targets. For $n_{eu}$ = $1.0\times10^{19}$ m$^{-3}$, the divertor region is mainly in the thermal force dominant regime ($|V_{||}^{fric}| < |V_{||}^{ther}|$), where the impurity ions are likely to transport to the upstream. While for $n_{eu}$ = $3.0\times10^{19}$ m$^{-3}$ in figure 5 (b), the thermal force is reduced while the intrinsic friction force is enhanced, and the intrinsic friction force dominant regime ($|V_{||}^{fric}| > |V_{||}^{ther}|$) has been attained especially near the divertor targets, where the impurity ions are likely to be pushed towards the divertor targets. Further, the distrbutions of neutral carbon to $C^{1+}$ ionization source for the case with $n_{eu}$=$1.0\times10^{19}$ m$^{-3}$ and $n_{eu}$=$3.0\times10^{19}$ m$^{-3}$ are shown in figure 6. The ionization sources locate at the area adjacent to the divertor targets. However, as the increment in $n_{eu}$, the ionization source for neutral carbon to $C^{1+}$ has shrunk closer to the divertor targets in figure 6. Hence, for the high density case, more ionization sources locate in the intrinsic friction force dominant region and the ionized carbon ions are likely to be confined. Therefore, it is seen that a better impurity screening can be achieved in the high density case.

The assessments of the impurity screening effect are illustrated in figures 7 and 8. Figure 7 displays the profiles of the total number of carbon ions with different charge states ($N_C^{m+}=\Sigma$ ($N_C^{1+}\sim N_C^{6+}$)) in space and the carbon impurity influx into the plasma ( $\Gamma_C$=*recycling flux*×*sputtering yield* ) against the $n_{eu}$. The increased $n_{eu}$ results in a higher recycling flux on the divertor targets, and hence, a larger eroded carbon influx as shown in figure 7. The $N_C^{m+}$ decreases with the enhancement of $\Gamma_C$ for $n_{eu}$ ≥$1.5\times10^{19}$ m$^{-3}$. The enhanced $n_{eu}$ would lead to a stronger intrinsic friction force in the divertor region as shown in figure 5, which drives the carbon impurity towards the divertor targets. Therefore, the dominant intrinsic friction force for high density scenarios can suppress the carbon leakage although more carbon impurity has been released from the divertor targets. On the other hand, the individual numbers of carbon ions for chemical erosion and physical sputtering are shown with dash lines in figure 7. It can be seen that the physically sputtered carbon impurity has a larger quantity than that induced by chemical erosion, since the energetic physically sputtered impurity can penetrate deeper into the plasma. Additionally, the average effective charge ($Z_{eff}$) is studied in figure 8, which is calculated with the equation $Z_{eff} = \sum n_i Z_i^2 / \sum n_i Z_i$. The subscript $i$ denotes different species including the background plasma ion ($D^+$) and impurity carbon ions ($C^{1+}$- $C^{6+}$). Figure 8 shows a clear reduction in $Z_{eff}$ as the $n_{eu}$ increases. The $Z_{eff}$ is about 2.8 for $n_{eu}$ = $1.0\times10^{19}$ m$^{-3}$, and drops rapidly to no more than 1.5 when $n_{eu}$ rises to $2.0\times10^{19}$ m$^{-3}$. The continuous increase on $n_{eu}$ leads to a further diminution of $Z_{eff}$. It can be seen that the $Z_{eff}$ becomes 1.04 for $n_{eu}$=$3.5\times10^{19}$ m$^{-3}$.

The 2D distributions of carbon impurity are studied in figures 9 and 10, which display the poloidal distributions for low and high density cases, respectively. For the low density case with $n_{eu}$=$1.0\times10^{19}$ m$^{-3}$, the $C^{1+}$ and $C^{2+}$ ions are mainly distributed in the divertor leg and private regions in figures 9 (a) and (b). The $C^{3+}$ and $C^{4+}$ ions can migrate to the upstream along the SOL as shown in figures 9 (c) and (d). The $C^{3+}$ ions are mainly in the SOL region, while the $C^{4+}$ ions are distributed around the separatrix. In addition, the $C^{5+}$ and $C^{6+}$ ions mainly populate inside the separatrix where has a high plasma temperature as shown in figures 9 (e) and (f). For the high density case with $n_{eu}$=$3.0\times10^{19}$ m$^{-3}$,the $C^{1+}$ and $C^{2+}$ ions in figures 10 (a) and (b) mostly populate the private region, while the densities of $C^{1+}$ and $C^{2+}$ ions in the divertor leg are much smaller than that for $n_{eu}$=$1.0\times10^{19}$ m$^{-3}$ due to the enhanced friction force. The $C^{3+}$ and $C^{4+}$ ions principally populate at the low-field side (LFS), while the high-field side (HFS) has fewer $C^{3+}$ and $C^{4+}$ ions in figures 10 (c) and (d). The $C^{5+}$ and $C^{6+}$ ions have similar distributions as the case of $n_{eu}$=$1.0\times10^{19}$ m$^{-3}$. Additionally, the densities of $C^{5+}$ and $C^{6+}$ inside the separatrix decrease with the enhanced $n_{eu}$, which also indicates that a better impurity screening can be achieved in the high density cases. The eroded neutral carbons are more likely to be ionized and trapped at the divertor region for high density scenarios.

Based on these results, a question related to the carbon source location is emerged that why the $C^{3+}$ and $C^{4+}$ ions principally populate at the LFS for $n_{eu}$=$3.0\times10^{19}$ m$^{-3}$ as shown in figures 10 (c) and (d). Further investigations have been attempted to make it clear. The EMC3-EIRENE code has a flexibility to switch on/off the impurity source on divertor targets. The outboard divertor target is divided into the outboard vertical target (OVT) and horizontal target (OHT), as shown in figure 11. A comparison with the impurity source location is displayed in figures 12. For figures 12 (a) and (b), the impurity source from the OHT switchs on, while for figures 12 (c) and (d), the OVT is switched on. Here, it should be noted that all the impurity sources on divertor targets are

switched on in the other figures except that in figure 12. As is shown in figures 12 (a) and (b), the LFS is no longer the concentrated region of carbon ions, which indicates that the carbon impurity eroded from the horizontal targets cannot penetrate deep into the SOL. On the contrary, figure 12 (c) and (d) suggest that the carbon impurity eroded from the vertical targets mainly populates the LFS. Therefore, the carbon impurity located at the SOL is derived from the OVT instead of the OHT. The physical reason can be illustrated in figure 1 (c) and figure 5. The larger flux expansion in HFS leads to a larger zone of low $T_e$ , which results in a wider intrinsic friction force dominant region at the inboard divertor leg compared to that at the outboard one in figure 5. More precisely, the intrinsic friction force dominant region near the OVT is too thin to prevent the leakage of carbon impurity.

### 4.4 Studies of the impurity power loss

The 2D distributions of impurity power loss for cases with $n_{eu}$ = 1.0 and 3.0 × $10^{19}$ $m^{-3}$ are shown in figure 13. It is noted that the figures 13 (a) and (b) have different ranged colorbars. For $n_{eu}$=1.0×$10^{19}$ $m^{-3}$, the power loss occurs in the divertor leg regions. While the power loss in the divertor leg region has been obviously suppressed and the main power loss zone locates close to the divertor targets when $n_{eu}$ increases to 3.0×$10^{19}$ $m^{-3}$. The evolution of power loss pattern is attributed to the distributions of carbon impurity density. It can be seen that the dominant radiation charge states ($C^{1+}$, $C^{3+}$, $C^{3+}$) are mainly populated in the divertor leg regions in figure 9 for $n_{eu}$=1.0×$10^{19}$ $m^{-3}$, which results the strong power loss in the divertor leg regions in figure 13 (a). When the $n_{eu}$ increases to 3.0×$10^{19}$ $m^{-3}$, the dominant radiation charge states are confined near the target and the penetration to divertor leg region has been prevented due to the enhanced intrinsic friction force as shown in figure 5. Thus, the power loss in the divertor leg regions has been reduced and main power loss zone locates near the divertor targets for $n_{eu}$=3.0×$10^{19}$ in figure 13 (b).

The profiles of total power loss and the contributions of different charge-state carbon ions are presented in figures 14 (a) and (b), respectively. The total power loss of carbon impurity is about 0.3 MW for $n_{eu}$=1.0×$10^{19}$ $m^{-3}$, and it increases rapidly to more than 0.6 MW for $n_{eu}$=1.5×$10^{19}$ $m^{-3}$. Moreover, continuous increase in $n_{eu}$ has been attempted, and the total power loss shows no significant differences, which remains at 0.6~0.7 MW. The contributions of chemically eroded and physically sputtered carbon impurities in total power loss have also analyzed in figure 14 (a). The profiles of impurity power loss show that the physically sputtered carbon impurity contributes more in the total power loss than the chemically eroded carbon impurity, resulting from the higher amount of physically sputtered carbon impurity as shown in figure 7. The detailed analysis of the individual power loss of carbon ions in different charge states has been indicates in figure 14 (b). When $n_{eu}$ increases from 1.0×$10^{19}$ to 1.5×$10^{19}$ $m^{-3}$, the power losses of all carbon ions ($C^{1+}$ ~ $C^{5+}$) are enhanced, which results the obvious increment in the total power loss. Nevertheless, the profiles of different charge-state carbon ions show different trends when continuous increase in $n_{eu}$ is attempted. The power loss of $C^{1+}$ increases rapidly with the increment of $n_{eu}$, which is enhanced from 25 kW to 280 kW when $n_{eu}$ increases from 1.5×$10^{19}$ to 3.0×$10^{19}$ $m^{-3}$. The profile of $C^{2+}$ is increasing when $n_{eu}$<2.5×$10^{19}$ $m^{-3}$ , and decreasing slowly when $n_{eu}$>2.5×$10^{19}$ $m^{-3}$. The power loss of $C^{3+}$ shows no siginificant difference as the $n_{eu}$ increases to higher than 1.5×$10^{19}$ $m^{-3}$. When $n_{eu}$ increases from 1.5×$10^{19}$ to 3.5×$10^{19}$ $m^{-3}$, the profiles of $C^{4+}$ and $C^{5+}$ decrease with the enhanced $n_{eu}$. In high density scenarios, most of the power exhaust is contributed by the low charge-state carbon ions ($C^{1+}$, $C^{2+}$, $C^{3+}$), while the $C^{4+}$ and $C^{5+}$ make little contributions. For instance, the $C^{4+}$ and $C^{5+}$ exhaust about 3% of the total impurity power loss in the case of $n_{eu}$=3.5×$10^{19}$ $m^{-3}$.

The power exhaust of carbon impurity is ultimately determined by the number of carbon ions and the background plasma conditions. As is displayed in figure 7, the total number of carbon ions decreases in high density cases. Futher, the carbon particle numbers of each charge states against the $n_{eu}$ have been conducted in figures 15 (a) and (b). The number of $C^{1+}$ increases slightly with the enhanced $n_{eu}$. While the $C^{2+}$ and $C^{3+}$ ions are reduced with the increment in $n_{eu}$. The profiles of $C^{4+}$, $C^{5+}$ and $C^{6+}$ exhibit similar trends against $n_{eu}$, which roll over when $n_{eu}$ = 1.5 ×$10^{19}$ $m^{-3}$. On the other hand, it can be seen that the numbers of high charge-state carbon ions are much larger than that of low charge-state carbon ions, especially for the low density cases. The normalized power loss ($P_{loss\_norm}^{C^{m+}} = P_{loss}^{C^{m+}} / N_{C^{m+}}$) is presented in figure 16 in order to reveal the impacts of background plasma condition. $C^{1+}$,$C^{2+}$ and $C^{3+}$ have obviously higher power loss efficiencies with the larger $n_{eu}$. The power loss efficiencies of high charge-state carbon ions ($C^{4+}$, $C^{5+}$) are slight compared with the high charge-state carbon ions ($C^{1+}$,$C^{2+}$ and $C^{3+}$) and show no significant differences with the enhanced $n_{eu}$. The high density cases with carbon impurities are better in power exhaust, since the total impurity power exhaust is mainly contributed by the low charge-state carbon ions ($C^{1+}$, $C^{2+}$, $C^{3+}$).

## 5. Summary

The edge plasma properties and the carbon impurity on the new tokamak HL-2M have been investigated with EMC3-EIRENE code, which is motivated to provide estimations on the edge plasma and impurity performance for HL-2M. The parameter scan of the upstream electron density has been performed to check the operation regime of HL-2M. For $n_{eu}$ = 1.0×$10^{19}$ $m^{-3}$, the low-recycling regime should be avoided because the high divertor plasma temperature and heat loads

on divertor targets can have a serious impact on the erosion and lifetime of divertor targets. The high-recycling regime can be accessible for $n_{eu} \geq 1.5\times10^{19}$ m$^{-3}$. Further, when the $n_{eu}$ increases to higher than $2.5\times10^{19}$ m$^{-3}$, the prior detachment regime is achieved, and it can be speculated that the detached edge plasma can be obtained for $n_{eu} \geq 4.0\times10^{19}$ m$^{-3}$ on HL-2M. Additionally, it has been found that the heat loads on the outboard divertor target is more intense due to the smaller deposition width.

The detailed analyses on the carbon impurity transport and its power exhaust property have been carried out. The intrinsic friction force dominant region expands as the $n_{eu}$ increases, where the carbon ions are driven towards the divertor targets. Thus, even though more carbon impurity has been released in the high density cases, a better impurity screening can be obtained. A futher study on the impacts of the impurity source location has been performed by dividing the outboard target into two individual parts, which indicates that the carbon impurity eroded from the vertical part of the outboard divertor target is more easily to transport through the thin intrinsic friction force dominant region and leak out into the upstream. As a result, there would be a carbon impurity build-up at the SOL of the low-field side even in the high density cases. The total power loss of carbon impurity shows no significant differences with the enhanced plasma density for the cases with $n_{eu} \geq 1.5\times10^{19}$ m$^{-3}$, though the total number of carbon ions obviously decreases. The investigations on carbon ions in each charge states suggests that the total power exhaust is mainly contributed by low charge-state carbon ions ($C^{1+}$, $C^{2+}$, $C^{3+}$), which have larger power loss efficiencies in the high density/low temperature scnarios.

The performance of intrinsic carbon impurity has been estimated in this work which is the first step in obtaining an insight into the impurity transport. In the future works, the comparative investigations between the effects of extrinsic impurity and intrinsic impurity will be performed on transport behaviors, power exhaust and heat flux reduction, etc[40,41]. On the other hand, the benchmarks with other studies [42] will be performed in the future, through which the impacts of drifts and current can be assessed.

## Acknowledgements

This work supported by National MCF Energy R&D Program of China Nos: 2017YFE0301206, 2018YFE0311100, 2018YFE0303105 and 2017YFE0300402, National Natural Science Foundation of China under Grant No. 12075047, High-level talent innovation support program of Dalian No. 2017RQ052.

## References

[1] Federici G. et al 2001 Nucl. Fusion 41 1967
[2] Loarte A. et al 2007 Nucl. Fusion 47 S203
[3] Fussmann G. 1986 Nucl. Fusion 26 983
[4] Pacher H.D. et al 1997 J. Nucl. Mater 241-3 255
[5] Pitcher C.S. and Stangeby P.C. 1997 Plasma Phys. Control. Fusion 39 779
[6] Roth J. et al 2009 J. Nucl. Mater. 390–1 1
[7] Lunt T. et al 2011 Plasma Phys. Control. Fusion 53 125010
[8] Kobayashi M. et al 2013 Nucl. Fusion 53 033011
[9] Kawamura G. et al 2018 Plasma Phys. Control. Fusion 60 084005
[10] Leonard A.W. et al 1997 Phys. Rev. Lett. 78 4769
[11] Kobayashi M. et al 2013 Nucl. Fusion **53** 093032
[12] Dai S.Y. et al 2016 Nucl. Fusion 56 066005
[13] Zhang H.M. et al 2015 Plasma Fusion Res. 10 3402038
[14] Kobayashi M. et al 2010 Phys. Plasmas **17** 056111
[15] Canik J.M. et al 2015 J. Nucl. Mater 463 569
[16] Reimold F. et al 2015 J. Nucl. Mater 463 128
[17] Li Q. and HL-2M Team 2015 Fusion Eng. Des. 96-97 338
[18] Liang Z. et al 2020 Fusion Eng. Des. 159 111803
[19] Liu D.Q. et al 2013 Fusion Eng. Des. 88 679
[20] Cai L.J. et al 2017 Fusion Eng. Des. 124 262
[21] Feng Y. et al 2004 Contrib. Plasma Phys. **44** 57
[22] Reiter D. et al 2005 Fusion Sci. Technol. **47** 172
[23] Feng Y. et al 2011 Plasma Phys. Control. Fusion 53 024009
[24] Frerichs H. et al 2013 J. Nucl. Mater. **438** S360 – 3
[25] Kobayashi M. et al 2015 Nucl. Fusion **55** 104021
[26] Dai S.Y. et al 2018 Nucl. Fusion **58** 096024
[27] Kobayashi M. et al 2017 Rev. Sci. Instrum. **88** 033501
[28] Frerichs H. et al 2012 Nucl. Fusion 52 054008
[29] Kawamura G. et al 2014 Contrib. to Plasma Phys. 54 437
[30] Feng Y. et al 1997 J. Nucl. Mater 243-243 930
[31] Reiter D. et al 2005 Fusion Sci. Technol., 47, 172
[32] Stangeby P.C. 2000 The Plasma Boundary of Magnetic Fusion Devices (Bristol: Institute of Physics Publishing)
[33] Eich T. et al 2013 Nucl. Fusion **53** 093031
[34] Dai S.Y. et al 2021 Plasma Phys. Control. Fusion 63 025003
[35] Liu B. et al 2019 Plasma Physics and Controlled Fusion 62 035003
[36] Roth J. et al 2004 Nucl. Fusion 44 L21–L25
[37] Stangeby P.C. et al 2020 Nucl. Fusion. 60 106005
[38] Senichenkov I Yu et al 2019 Plasma Phys. Control. Fusion **61** 045013
[39] Sytova E. et al 2019 Nucl. Mater. Energy 19 72
[40] Lore J.D. et al 2015 J. Nucl. Mater. 463 515–518
[41] Liu B. et al 2020 Plasma Phys. Control. Fusion. 62
[42] Sytova E. et al 2018 Contrib. Plasma Phys. 58 622

The figures and table are shown in the follow:

Table 1. The sputtering coefficients for scenarios with different $n_{eu}$

| $n_{eu}$ ($10^{19}$ $m^{-3}$) | 1.0 | 1.5 | 2.0 | 2.5 | 3.0 | 3.5 |
|---|---|---|---|---|---|---|
| *Sputtering yield* | 0.035 | 0.03 | 0.025 | 0.02 | 0.015 | 0.01 |

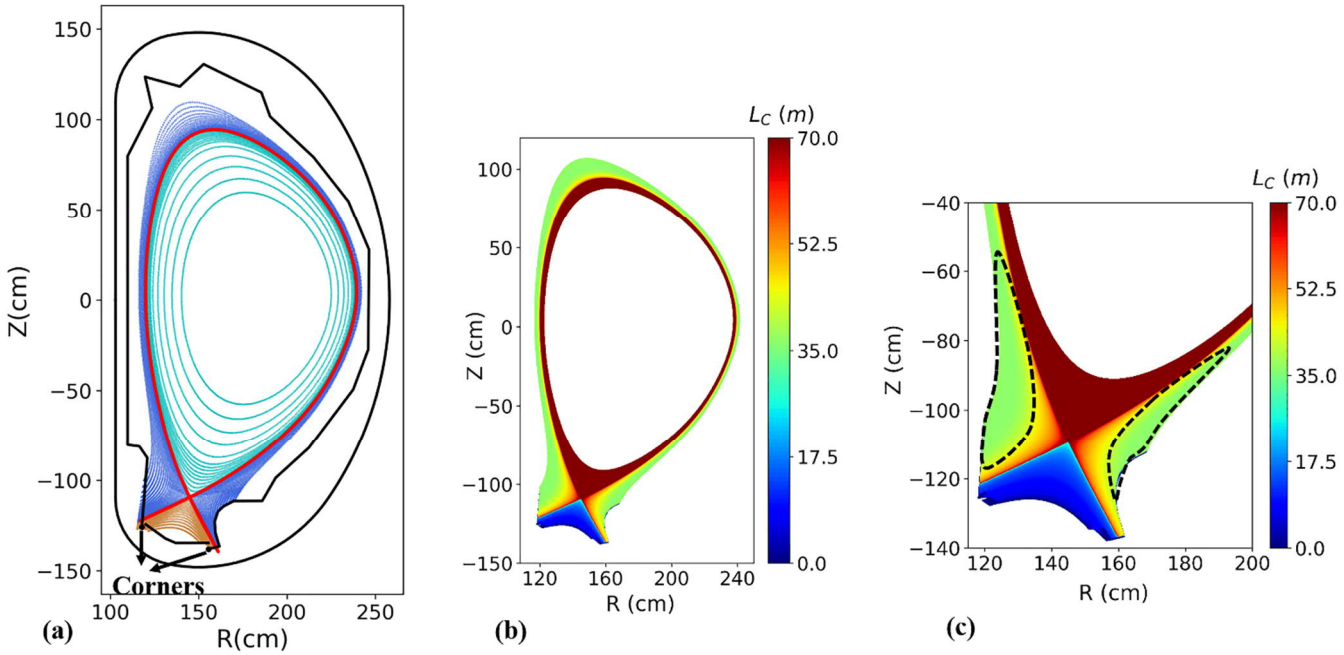


Fig 1. (a).The poloidal cross section of the computational mesh. The modelled domain of the edge plasma comprises three zones: 'Core': the region inside the separatrix is represented with light blue; 'SOL': the region including the SOL and divertor is represented with dark blue. 'PFR': the private flux region is displayed with brown. The toroidal resolution of computational mesh is 2.8125° for all three zones. In radial and poloidal directions, the 'Core' has 15×500 (radial×poloidal) grids, the 'SOL' is divided into 23×673 grids, and the 'PFR' has 15×174 grids. The vessel vacuum and targets are also shown as thick dark lines. The marked points (Corners) are each corners of the divertor targets. (b). The contour plot of connection length. (The connection length in core is infinite). (c). A zoom-in view of connection length in the divertor region.

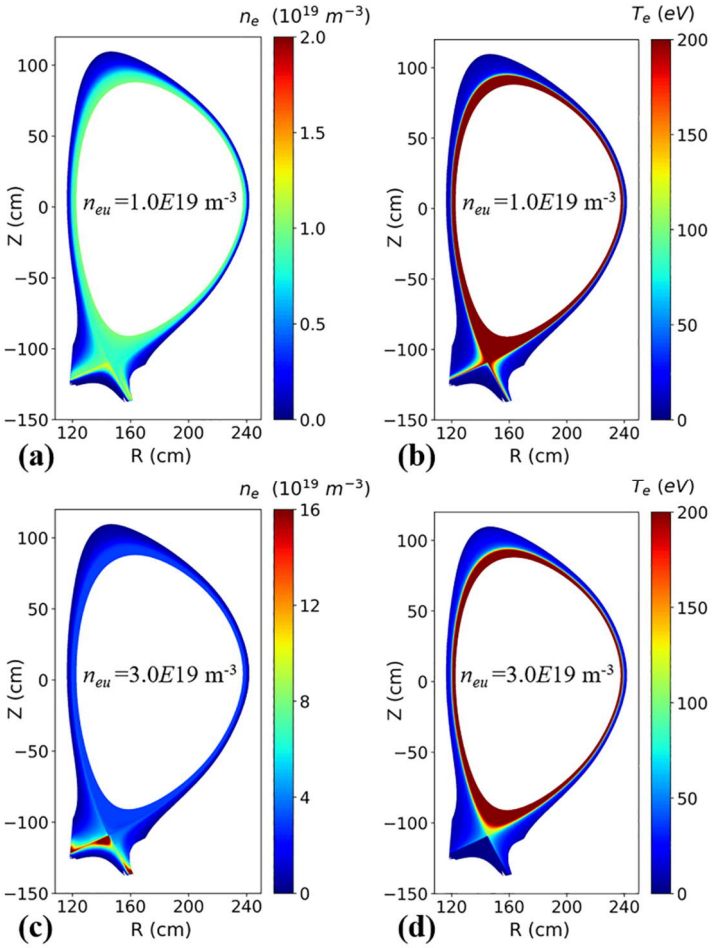


Fig 2. The 2D distributions of (a) (b) electron density and (c) (d) electron temperature for low/high density cases.

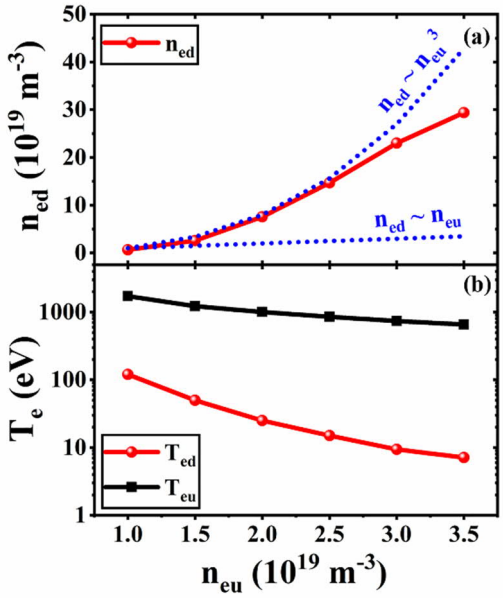


Fig3. The profiles of (a) downstream electron density. (b) electron temperature.

[在此处键入]

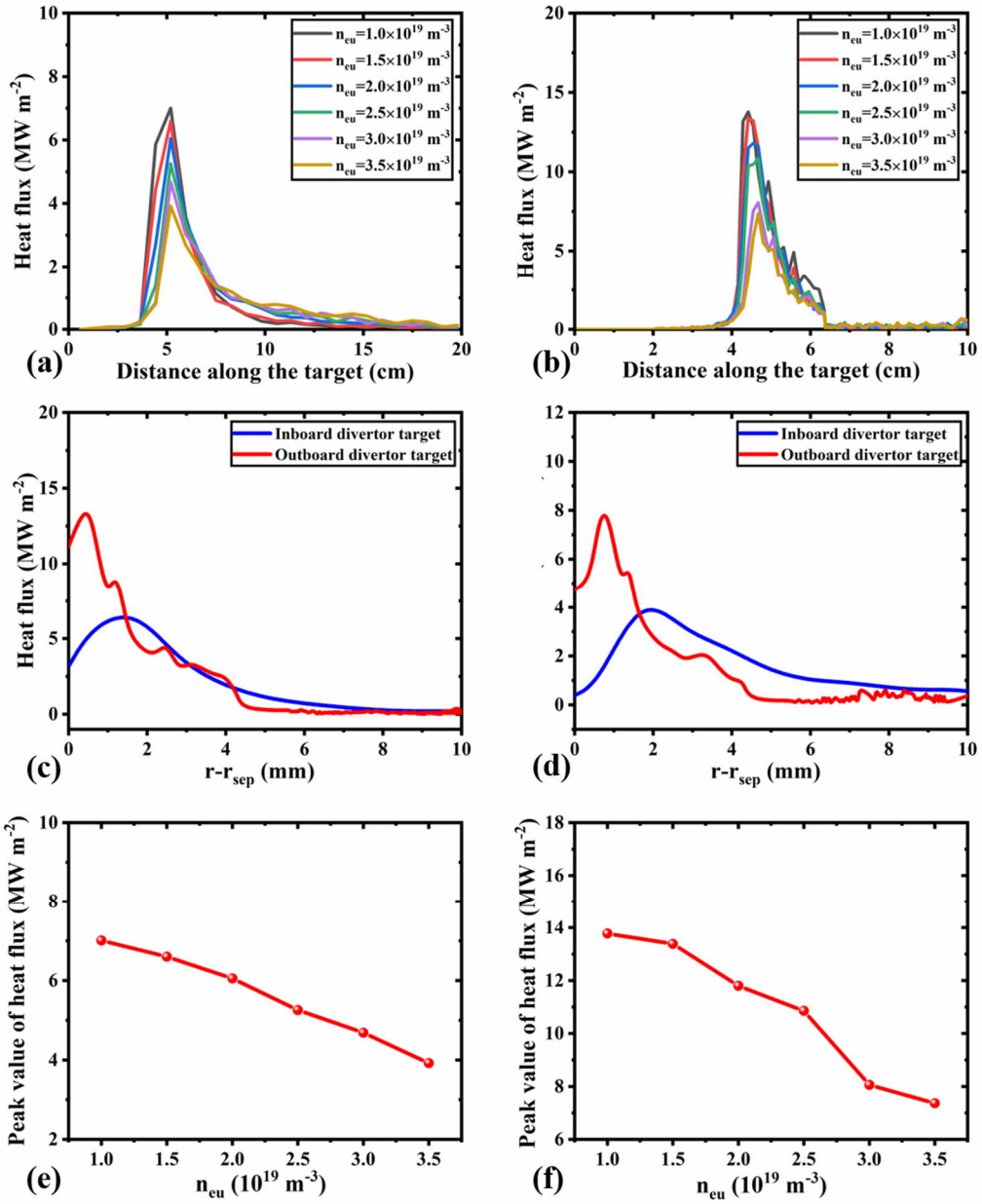


Fig 4. (a) (b) The distributions of heat loads on the in- and out- board divertor targets. (c) (d) The heat flux profiles on the in- and out- board divertor targets mapped to the outside midplane for $n_{eu}$ = 1.0×10$^{19}$ and 3.0×10$^{19}$ m$^{-3}$. (e) (f) The peak values of heat loads on the in- and out- board divertor targets.

[在此处键入]

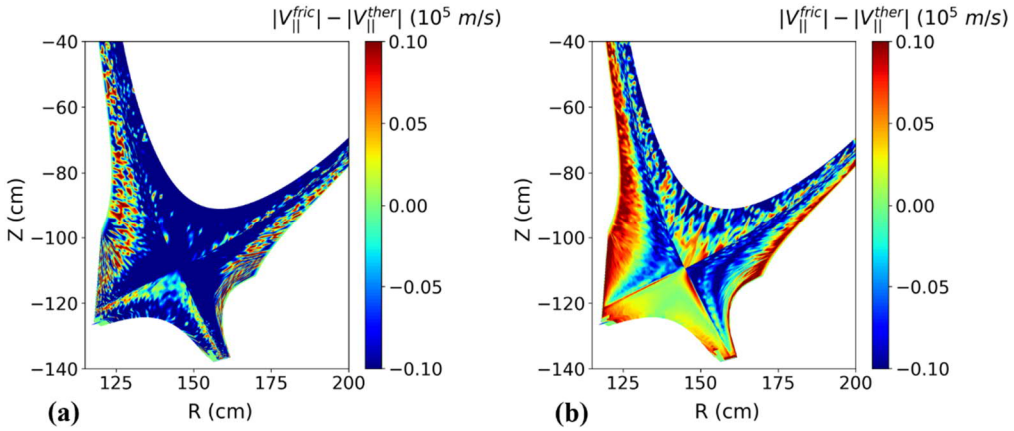


Fig 5. The distributions of impurtity velocity for the cases with (a) $n_{eu}$ = 1.0×10$^{19}$ m$^{-3}$ and (b) $n_{eu}$ = 3.0×10$^{19}$ m$^{-3}$

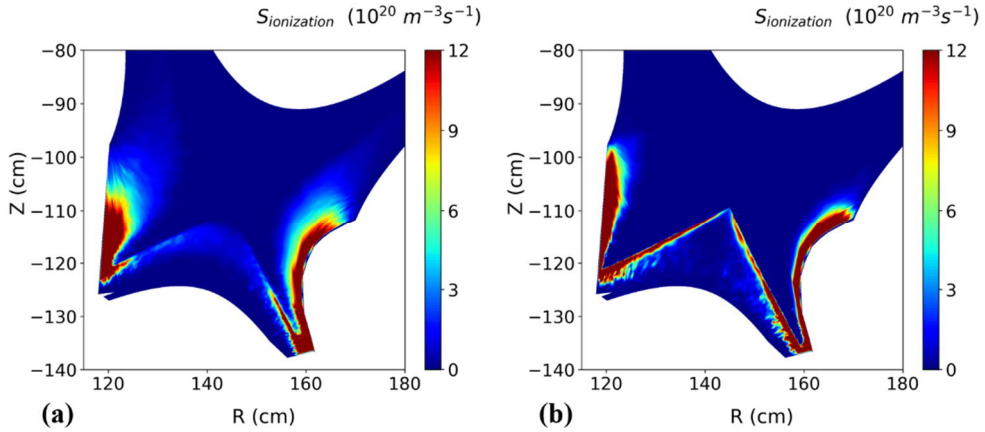


Fig 6. The distributions of neutral carbon to $C^{1+}$ ionization source for the cases with (a) $n_{eu}$ = 1.0×10$^{19}$ m$^{-3}$ and (b) $n_{eu}$ = 3.0×10$^{19}$ m$^{-3}$

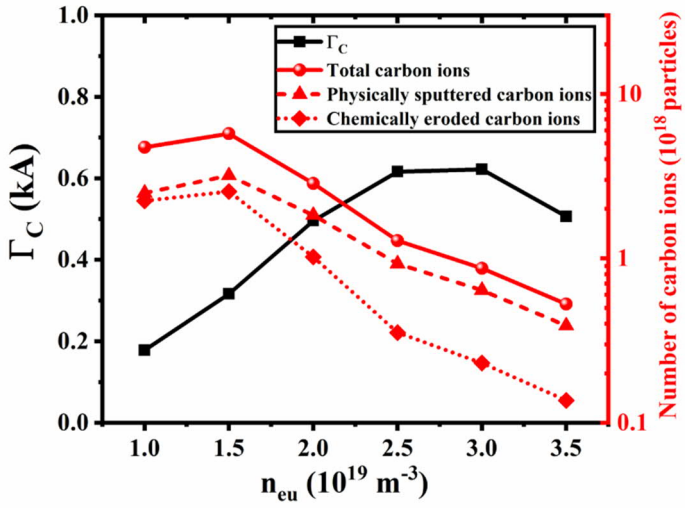


Fig 7. The functions of influx of carbon impurity and the number of carbon ions against $n_{eu}$

[在此处键入]

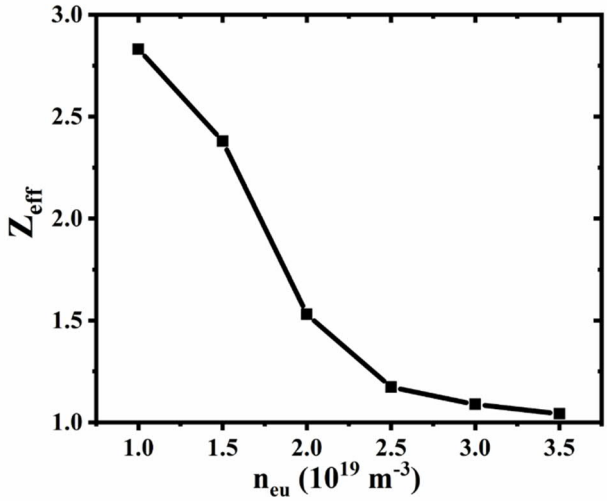


Fig 8. The functions of the effective charge ($Z_{eff}$) against $n_{eu}$

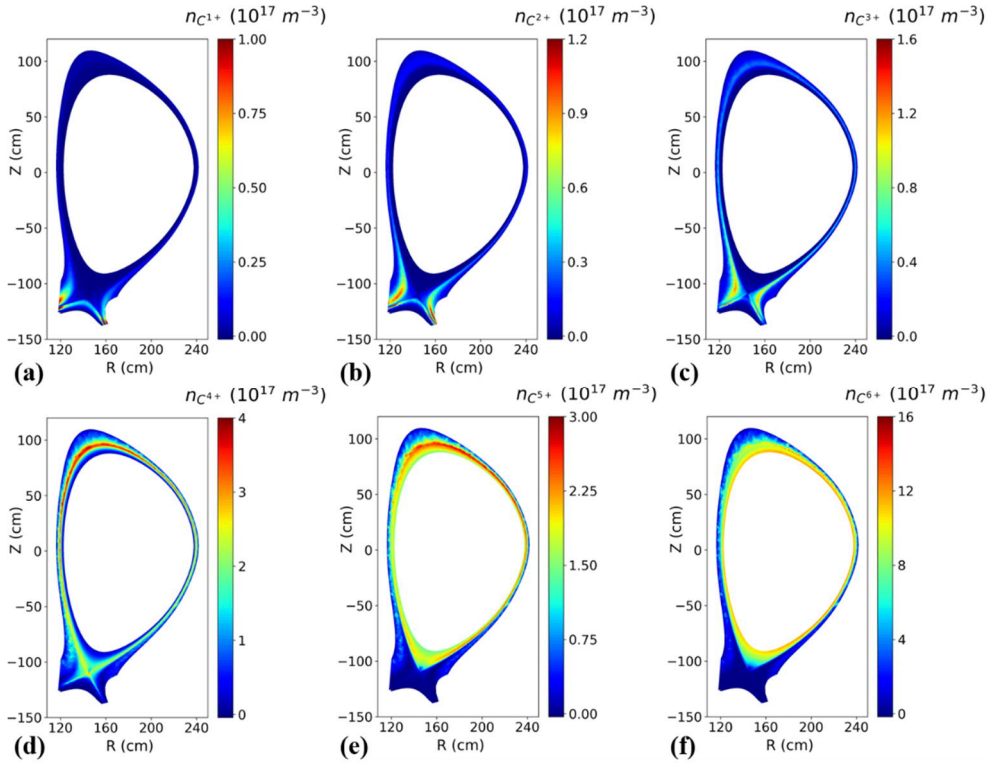


Fig 9. The 2D distributions of carbon ions for scenario with $n_{eu}$=1.0×$10^{19}$ $m^{-3}$

[在此处键入]

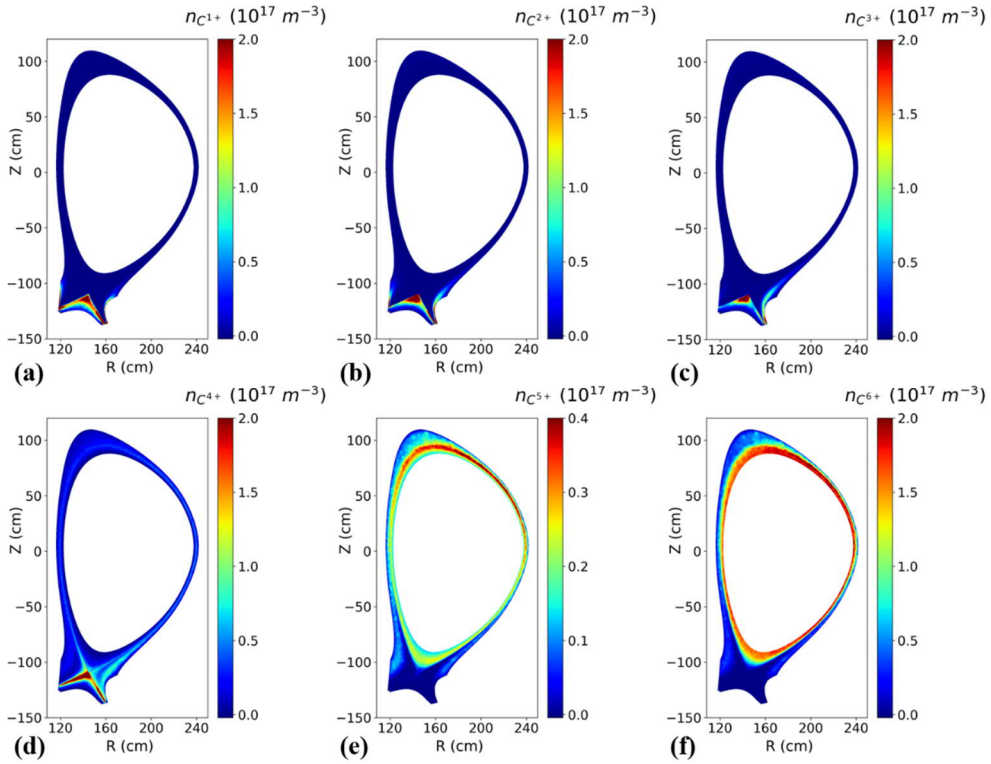


Fig 10. The 2D distributions of carbon ions for scenario with $n_{eu}$=3.0×$10^{19}$ $m^{-3}$

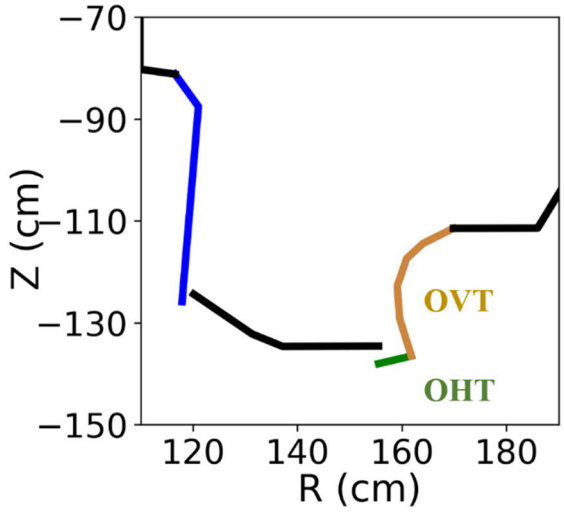


Fig 11. The schematic of partitioning target.

[在此处键入]

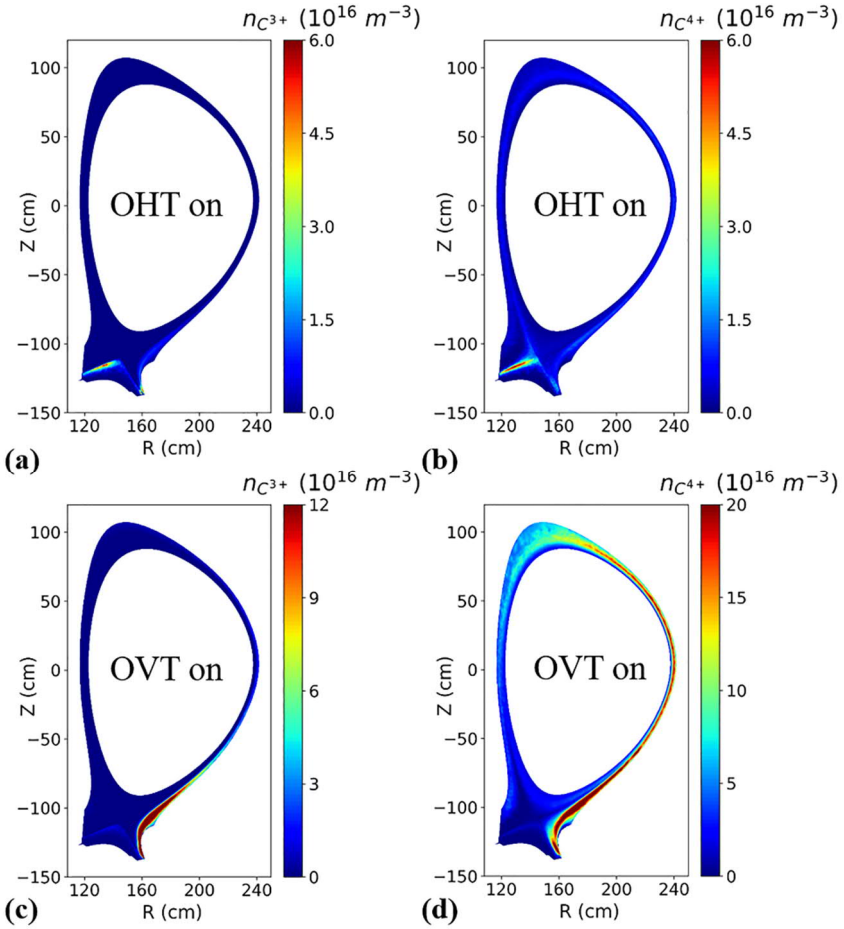


Fig 12. The distrbutions of $C^{3+}$ and $C^{4+}$ for OHT/OVT switched on.

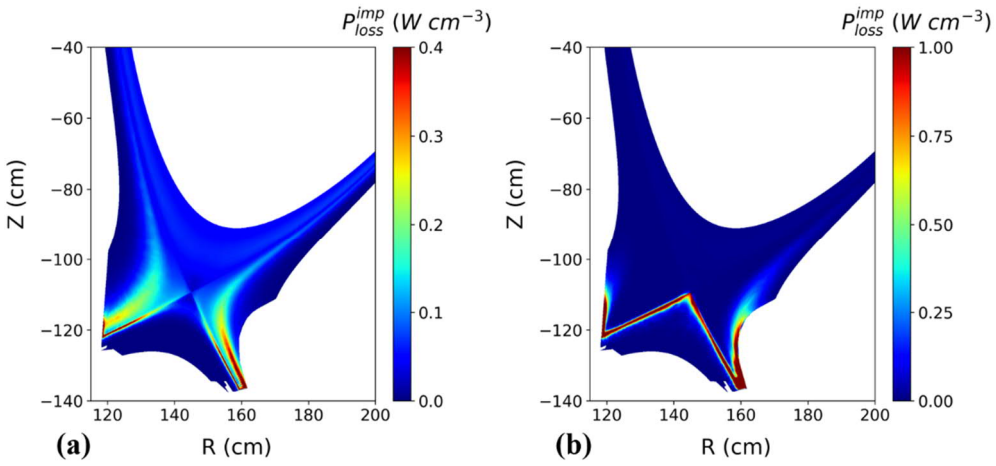


Fig 13. The 2D distributions of impurity power loss for cases with (a) $n_{eu}$ = 1.0×$10^{19}$ $m^{-3}$ and (b) $n_{eu}$ = 3.0×$10^{19}$ $m^{-3}$

[在此处键入]

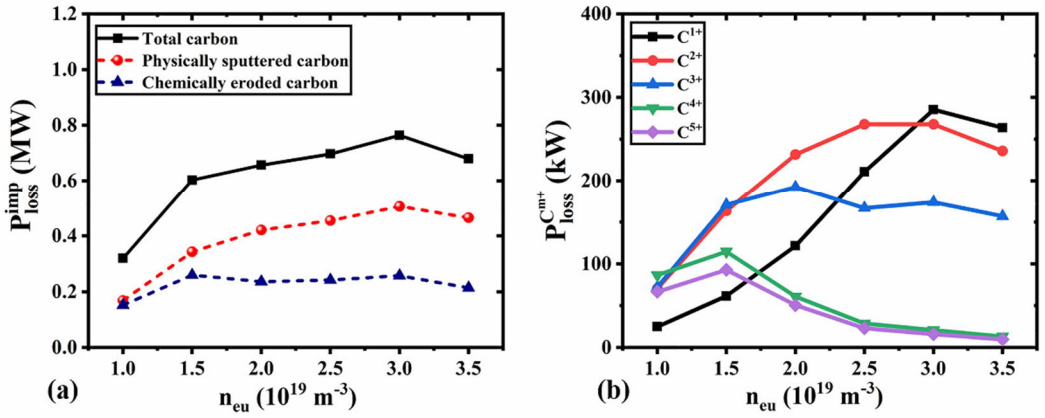


Fig 14. (a) The profile of the total power loss of carbon ions. (b) The profiles of individual power losses of carbon ions with different charge states.

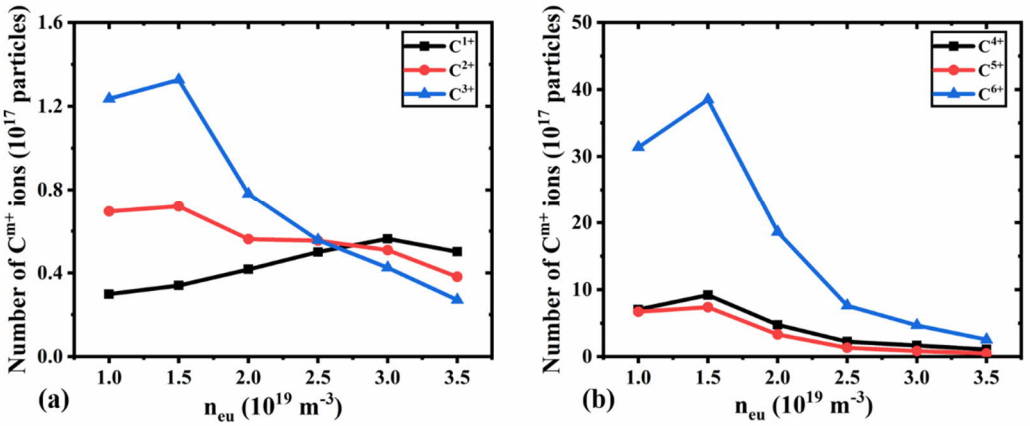


Fig 15. The numbers of carbon ions with different charge states. (a) $C^{1+}$,$C^{2+}$ and $C^{3+}$ (b) $C^{4+}$, $C^{5+}$ and $C^{6+}$

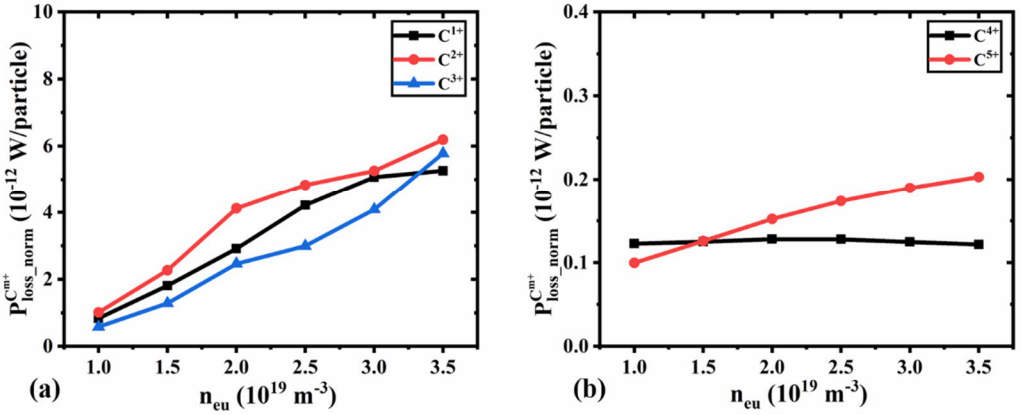


Fig 16. The normalized power losses for (a) $C^{1+}$, $C^{2+}$, $C^{3+}$ (b) $C^{4+}$, $C^{5+}$

[在此处键入]